nature photonics

ARTICLES

https://doi.org/10.1038/s41566-019-0387-5

Anisotropic structural dynamics of monolayer crystals revealed by femtosecond surface X-ray scattering

I-Cheng Tung[1], Aravind Krishnamoorthy[2], Sridhar Sadasivam[3], Hua Zhou[1], Qi Zhang[1], Kyle L. Seyler[4], Genevieve Clark[4], Ehren M. Mannebach[5], Clara Nyby[6], Friederike Ernst[7,8], Diling Zhu[9], James M. Glownia[9], Michael E. Kozina[9], Sanghoon Song[9], Silke Nelson[9], Hiroyuki Kumazoe[10], Fuyuki Shimojo[10], Rajiv K. Kalia[2], Priya Vashishta[2], Pierre Darancet[3], Tony F. Heinz[7,8,11], Aiichiro Nakano[2], Xiaodong Xu[4], Aaron M. Lindenberg[5,8,11] and Haidan Wen[1]*

Ultrafast X-ray scattering is one of the primary tools to track intrinsic crystallographic evolution with atomic accuracy in real time. However, its application to study nonequilibrium structural properties at the two-dimensional limit remains a long-standing challenge due to a significant reduction of diffraction volume and complexity of data analysis. Here, we report femtosecond surface X-ray diffraction in combination with crystallographic model-refinement calculations to quantify the ultrafast structural dynamics of monolayer WSe_2 crystals supported on a substrate. We found the absorbed optical photon energy is preferably coupled to the in-plane lattice vibrations within one picosecond whereas the out-of-plane lattice vibration amplitude remains unchanged during the first ten picoseconds. The model-assisted fitting suggests an asymmetric intralayer spacing change upon excitation. The observed nonequilibrium anisotropic structural dynamics agrees with first-principles modelling in both real and momentum space, marking the distinct structural dynamics of monolayer crystals from their bulk counterparts.

The development of van der Waals (vdW) materials has opened up possibilities for the exploration of new physics in the two-dimensional (2D) limit[1,2]. Strong light–matter interaction in 2D materials allows optical control of electronic, spin and valley degrees of freedom, in which the structure of 2D materials is usually approximated to be stationary with weak optical excitation. With increasing optical excitation strengths, nonlinear processes start to occur[3–5] and the Born–Oppenheimer approximation may not be applicable. In addition, towards the monolayer limit, the influence of the surrounding environment on the properties of 2D systems becomes increasingly important[6–8]. For example, the anomalously large thermal conductivity of graphene may find applications in efficient thermal removal[9,10]. Unconventional interface superconductivity was ascribed to the unique electron–phonon coupling at the FeSe/$SrTiO_3$ interface[11], and unusual exciton–phonon interactions were observed across the interface of vdW heterostructures as well as between monolayer semiconductors and crystalline substrates[12,13]. In contrast to many investigations of unique electronic, spin, thermal and optical properties of 2D materials and at their interfaces, limited knowledge of the associated structural dynamics has been obtained. Understanding of the nonequilibrium structure–property relationship in these emergent 2D phenomena beyond thin films[14] calls for a direct quantitative measurement of the lattice dynamics of monolayer crystals at and across crystalline interfaces on ultrafast timescales.

With advances in generating ultrabright and ultrashort electron and X-ray pulses, tracking atomic structural dynamics in 2D materials on femtosecond timescales becomes possible. For example, ultrafast electron diffraction (UED) and microscopy were used to measure transient structural changes in various multilayer systems[15–19] and at surfaces[8,20,21]. At the monolayer limit, in-plane structural dynamics of monolayer crystals was characterized by UED in a transmission geometry[22,23], whereas the out-of-plane structural dynamics of a monolayer crystal was only inferred[23]. Complementary to UED, ultrafast X-ray diffraction has been widely used for studying structural dynamics in thin-film form, such as in the transition metal chalcogenides[14] and dichalcogenides[24]. If applied to surfaces, ultrafast surface X-ray scattering could provide direct and quantitative measurements of structural changes by recording diffraction profiles with non-zero momentum transfer along the out-of-plane direction, in contrast to techniques that measure only in-plane diffraction peaks or surface-sensitive optical probes close to the Brillouin zone centre[25]. But the direct structural characterization of non-equilibrium processes within a monolayer crystal using X-rays remains a challenge due to the significantly reduced scattering volume. Ultrafast three-dimensional atomic-scale rearrangements

[1]Advanced Photon Source, Argonne National Laboratory, Argonne, IL, USA. [2]Collaboratory of Advanced Computing and Simulations, University of Southern California, Los Angeles, CA, USA. [3]Center for Nanoscale Materials, Argonne National Laboratory, Argonne, IL, USA. [4]Department of Physics, University of Washington, Seattle, WA, USA. [5]Department of Materials Science and Engineering, Stanford University, Stanford, CA, USA. [6]Department of Chemistry, Stanford University, Stanford, CA, USA. [7]Department of Applied Physics, Stanford University, Stanford, CA, USA. [8]PULSE Institute, SLAC National Accelerator Laboratory, Menlo Park, CA, USA. [9]SLAC National Accelerator Laboratory, Menlo Park, CA, USA. [10]Department of Physics, Kumamoto University, Kumamoto, Japan. [11]Stanford Institute for Materials and Energy Sciences, SLAC National Accelerator Laboratory, Menlo Park, CA, USA. *e-mail: wen@anl.gov

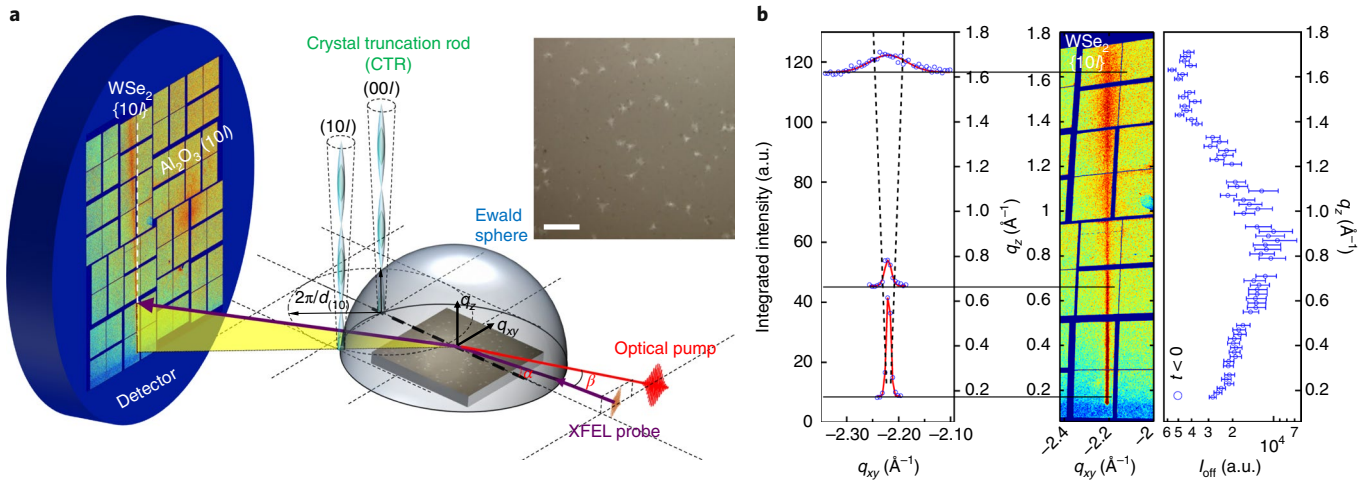

Fig. 1 | Experimental set-up and static surface X-ray diffraction. a, A schematic diagram of femtosecond surface X-ray diffraction. The (00*l*) and (10*l*) rods are shown representatively across the Ewald sphere. The X-ray probe beam strike on the sample close to grazing incidence ($\alpha = 1°$) and the optical pump beam is overlapped with the X-ray beam with a horizontal crossing angle $\beta = 5°$. The inset shows the optical images of the sample surface. Scale bar is 30 μm. The white dashed line shows a vertical line on the detector. **b**, Centre: corrected reciprocal space map around the off-specular {10*l*} rod. Left: the measured (blue circles) rod profiles with Gaussian fits (red) at various q_z values. The dashed lines that connect the curves at approximately their full-width at half-maximum is drawn as a guide to the eye. Right: integrated intensity as a function of q_z for the ground state {10*l*} CTR, obtained by integration over q_{xy}.

of monolayer crystals on supporting substrates, the most common platform of 2D phenomena and configuration of 2D devices, have not yet been mapped out.

In this Article, we report the first femtosecond surface X-ray diffraction (fSXD) study of monolayer crystals, which was enabled by the ultrahigh single-pulse brightness and ultrashort pulse durations of hard X-ray radiation of free electron lasers at the Linac Coherent Light Source (LCLS). Monolayer WSe_2 was chosen as the model system because it hosts strong exciton–phonon coupling with substantial impact in valley exciton dynamics[26,27], ultrafast dynamics[4,28], unusual exciton–interfacial phonon interactions at the vdW interface[12,13], and unique chiral phonons[29], and its X-ray scattering cross-section is relatively large in the family of transition metal dichalcogenides. In combination with crystallographic model-refinement calculations, we captured the lattice motions of monolayer WSe_2 along both in-plane and out-of-plane directions upon optical excitation. In particular, we found direct structural evidence of an anisotropic energy relaxation pathway that favours electron–phonon coupling along the in-plane direction occurring on a timescale of 1 ps, subsequently followed by an in-plane lattice expansion. In contrast, the out-of-plane lattice vibration remains unchanged within the measurement window of 10 ps. The anisotropic response agrees with first-principles simulations performed in real and momentum spaces, illuminating a key process of anisotropic nonequilibrium lattice dynamics in monolayer crystals. In addition, the model-assisted fitting suggests that the intralayer spacing changes in monolayers are asymmetric, in contrast to a symmetric intralayer compression of bulk WSe_2 on picosecond timescales, underlying a distinct structural response of monolayer crystals on a supporting substrate. The demonstrated methods unlock the benefit of surface-sensitive X-ray scattering to quantitatively measure ultrafast structural dynamics in atomically thin materials and across interfaces.

In-plane structural dynamics

We first characterized the sample at steady state by surface X-ray scattering (Fig. 1a). The samples are WSe_2 monolayer crystals with an averaged flake size of a few micrometres homogeneously covering the sapphire (Al_2O_3) substrate (see Methods). Since the crystal dimension is highly confined along the out-of-plane direction, its Fourier transformation in the reciprocal space shows as a vertical streak pattern along the crystal truncation rod (CTR) of a both-side 'truncated' crystal[30] (see Methods). The in-plane random orientations of WSe_2 flakes permit recording the off-specular {10*l*} CTR, the sum of (10*l*) and (01*l*) rods, on the area detector without rotating the sample, simultaneously measuring the diffraction intensity distribution along the in-plane (q_{xy}) and out-of-plane (q_z) momentum transfer direction in reciprocal space. The in-plane intensity profile of the {10*l*} rod was well fitted by a Gaussian shape with width increasing at higher q_z, indicating rippling of the monolayer crystals (Fig. 1b)[31,32] and possible microscale strain around defects.

The structural dynamics was measured by surface X-ray diffraction after optical excitation by 650 nm light pulses using pump–probe technique (see Methods). To study the in-plane dynamics, we integrated the diffraction intensity along q_z in the range 0.16–0.5 Å^{-1} (Fig. 1b) to obtain the diffraction intensity profile projected onto the q_{xy} axis. Time-dependent intensity profiles are plotted as a function of delay in Fig. 2a. The asymmetric wave-like differential profile (solid black curve in Fig. 2b) indicates a diffraction intensity reduction and a rod position shift to lower q_{xy} axis after excitation.

The {10*l*} Bragg rod position and intensity can be extracted as a function of time. Following optical excitation, we observed a decrease in diffracted intensity as a result of the Debye–Waller effect that can be fitted to an exponential function $\Delta I(t) \sim A[1-\exp(-t/\tau)]$ with amplitude A and time constant τ (blue curves, Fig. 2c). The in-plane electron–phonon coupling time $\tau = 0.8 \pm 0.4$ ps is faster than 1.83 ± 0.13 ps in bulk WSe_2[17]. The slowing down of energy coupling to the in-plane lattice vibration in the bulk may have multiple origins, including a lower defect density and indirect bandgap in the bulk, all of which can reduce electron–phonon scattering rates. The magnitude of 0.9% reduction of the diffraction intensity of {10*l*} rods corresponds to $\Delta\left\langle u_{xy}^2 \right\rangle = [\ln(I_0/I)]/q_{xy}^2 = 0.0018$ Å^2, where I_0 and I are the diffraction intensity before and after the excitation[16], and $\langle u_{xy} \rangle$ represents the mean square displacement along either x or y directions, assuming isotropic in-plane atomic displacement. The increase of $\left\langle u_{xy}^2 \right\rangle$ corresponds to an in-plane lattice temperature increase of 88 K, consistent with the estimated temperature rise from the absorbed energy (Supplementary Note 3). The time-dependent change of the CTR position was determined by fitting

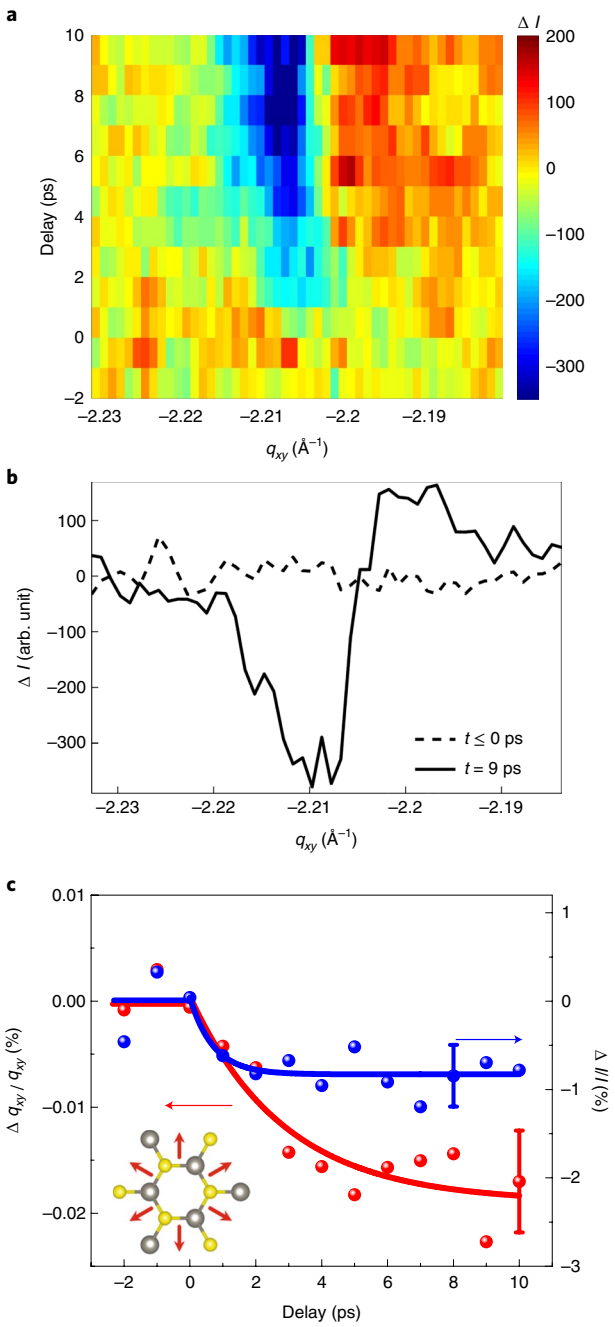

Fig. 2 | In-plane structural dynamics. a, Time-dependent differential diffraction intensity as projected to the q_{xy} axis integrated in the range $q_z = 0.16 - 0.5$ Å^{-1}. **b**, The differential diffraction intensity profile as a function of q_{xy} before and after optical excitation. **c**, Time-dependent in-plane rod position shift $\Delta q/q_0$ and diffraction intensity change $\Delta I/I_0$ of the {10*l*} reflection. The solid lines are fits presented in the text. The error bars represent the fitting errors.

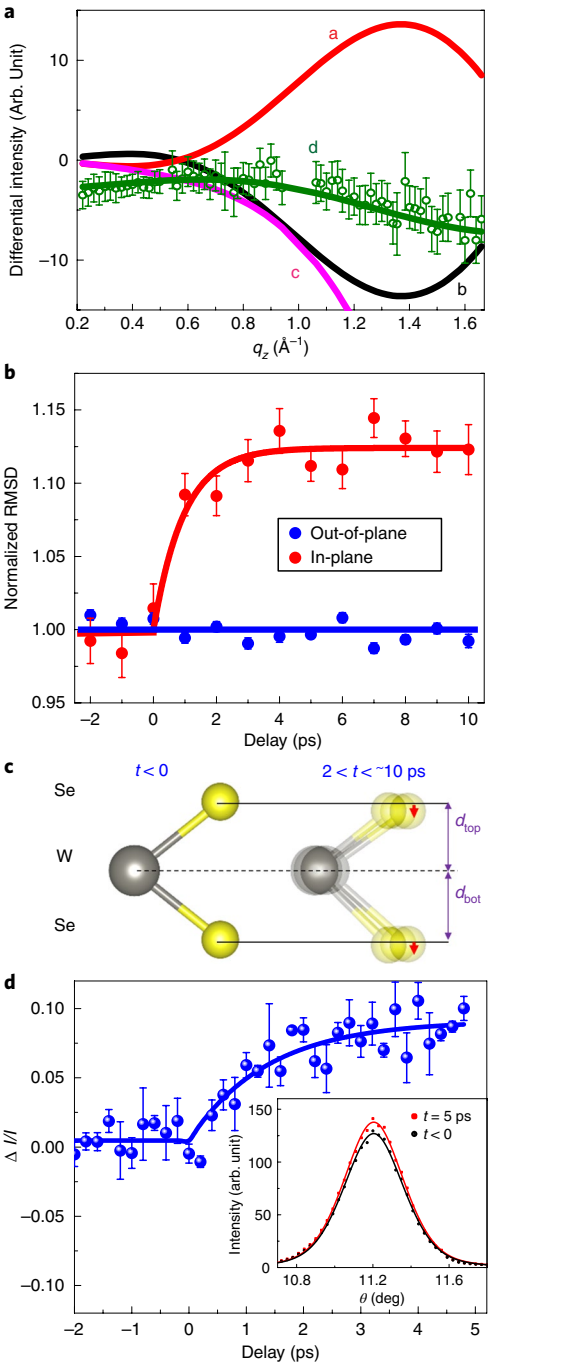

Fig. 3 | Out-of-plane structural dynamics. a, Differential X-ray scattering intensity profile of WSe_2 monolayers along the {10*l*} rod for $5 \leq \Delta t \leq 10$ ps. The solid lines are model calculations discussed in the text. **b**, Normalized in-plane and out-of-plane RMSD of WSe_2 monolayers. The error bars are the standard deviation of the fitting parameters in all fitting trials. Solid curves are guides to the eye. **c**, Schematic diagram of the atomic structure model of monolayer WSe_2. The blurriness of atom positions indicates the increase of the in-plane RMSD. The red arrows show the possible intralayer distance changes. **d**, The diffraction intensity change of the 004 Bragg peak of a bulk WSe_2 crystal upon optical excitation. The error bars show the standard errors of consecutive scans. The inset shows the rocking curve with fits before and 5 ps after optical excitation.

a 1D Gaussian profile to the {10*l*} rod intensity as projected to q_{xy} axis. The peak position shifts as a function of time can be described by a one-exponential function $\Delta q(t) \sim A[1-\exp(-t_q/\tau_1)]$ (red curve, Fig. 2c). The time constant of $\tau_1 = 2.9 \pm 1.2$ ps shows the characteristic time of the in-plane lattice expansion, as a result of an in-plane acoustic wave propagation[22,23]. Oscillatory local modes are missing, different from those observed in the freestanding multilayer samples[18,19]. These modes can be overdamped due to the interaction with the substrate at the monolayer limit. In addition, they are spatially averaged by the large X-ray probe so that the X-ray diffraction measurement shows the overall in-plane lattice expansion and effective Debye–Waller effect.

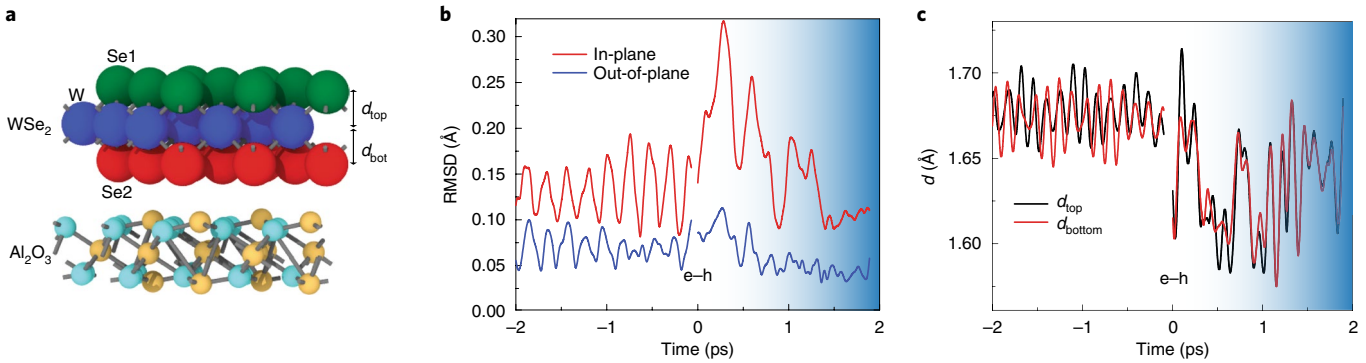

Fig. 4 | NAQMD simulations. a, Schematic of the simulated system: WSe_2 monolayer supported on an Al_2O_3 substrate. **b**, The in-plane and out-of-plane RMSD of all atoms before and after electronic excitation, respectively. 'e–h' represents electron–hole injection at time zero with a carrier density of 2.6×10^{14} cm^{-2}. The blue region represents the coupling of the monolayer with the thermostat. **c**, The intralayer spacing of W–Se atomic planes before and after electronic excitation.

Out-of-plane structural dynamics

The out-of-plane lattice dynamics was studied by comparing the measured CTRs with crystallographic model-refinement calculations of the diffraction intensity change along q_z as a function of time. By subtracting the ground-state CTR (Fig. 1b) from the excited-state CTR recorded at each delay, we obtained the time-dependent differential CTR along the {10l} rod. A representative differential CTR is shown as circles in Fig. 3a. The differential intensity is below zero, indicating a loss of total diffraction intensity as a result of the increase of incoherent lattice vibrations. The differential intensity varies as a function of q_z, with a minimal change around $q_z=0.7$ Å^{-1}. To qualitatively understand this q_z dependence, we compared the measured differential CTRs with calculated ones. A systematical study of differential CTRs as a function of various structural parameters can be found in Supplementary Note 2. The representative differential CTRs from four scenarios are shown in Fig. 3a: the intralayer spacing symmetrically expands (a) or contracts (b) by 0.2% without an root mean square displacement (RMSD) increase; the out-of-plane (c) and in-plane (d) RMSD increase of 10% without d-spacing change. It is clear that only scenario (d) matches the data well. This comparative study indicates that the energy relaxation is preferable along the in-plane direction and a symmetric intralayer d-spacing change does not agree with the measurement. The magnitude of RMSD change and intralayer spacing change as used in the calculation will be justified later.

To quantify the RMSD increase as a function of time, least-squares fitting was performed on the differential CTRs with the monolayer WSe_2 structure parameters allowed to vary (see Supplementary Note 1,2). Differential CTRs were fitted with two parameters, the percentage changes of in-plane and out-of-plane RMSDs ($\sqrt{\langle u^2\rangle}/\sqrt{\langle u_0^2\rangle}$), where $\sqrt{\langle u^2\rangle}$ is the measured RMSD of the transient structure, and $\sqrt{\langle u_0^2\rangle}$ is the calculated value of the ground state (see Supplementary Note 4). The intralayer spacing change was fixed for simplicity (see Supplementary Note 2) and will be treated in more detail in the Discussion section. From the model-assisted analysis of the X-ray scattering intensity profiles along {10l}, we experimentally determined the corresponding mean square displacements shown in Fig. 3b. Consistent with the qualitative analysis, the out-of-plane RMSD remains almost the same within 10 ps, whereas the in-plane RMSD increases by 12%, which corresponds to a 0.007 Å increase of the in-plane RMSD. The rise time is consistent with the blue curve in Fig. 2c. This anomalous structural response is suggestive of a strong anisotropy of energy relaxation pathways.

First-principles simulations

To give insight into the observed anisotropic energy relaxation pathway, we first performed nonadiabatic quantum molecular dynamics (NAQMD) simulations using the model shown in Fig. 4a. NAQMD follows the trajectories of all atoms, while describing electronic excitations and nonadiabatic transitions between excited electronic states assisted by atomic motions based on time-dependent density functional theory and surface-hopping approaches, which enables it to describe photoexcitation dynamics involving the coupled motion of electrons and nuclei[33].

Electronic excitation was simulated by the instantaneous creation of electron–hole pairs in the monolayer-substrate simulation cell at time zero. Figure 4b shows the calculated RMSD averaged over all atoms in the WSe_2 monolayer as a function of time at simulated electron–hole concentrations of 0 cm^{-2} (that is no excitation) and 2.6×10^{14} cm^{-2} respectively. Whereas the out-of-plane RMSD remains close to 0.08 Å, independent of excitation, the in-plane RMSD increases strongly to over 0.3 Å approximately 300 fs after instantaneous electronic excitation. The magnitude of the in-plane RMSD increase in the simulation normalized to the electron density is in agreement of the measured value since the excitation strength of simulated e–h density 2.6×10^{14} cm^{-2} is twenty times higher than that of 1.3×10^{13} cm^{-2} used in the experiments. We note that the in-plane lattice response relaxes to the ground state within 1.5 ps due to the coupling of the WSe_2 monolayer to the Nose–Hoover thermostat at 300 K. The use of a Nose–Hoover thermostat is required to stabilize the MD simulation. The coupling with the thermostat unavoidably exaggerates the energy relaxation rate so that the relaxation of RMSD occurs on an artificially fast timescale.

We note that the lateral size of the WSe_2 crystal of <1 nm in the NAQMD simulation is much smaller than the rippling domain size of 10 nm, so nanoscale rippling effects were not taken into account. Complementary to NAQMD simulations, we tracked phonon populations of all vibrational modes as a function of time by calculating electron–phonon and third-order phonon–phonon interactions[34] (Supplementary Note 5). The rippling effect was captured in these analytical calculations through the inclusion of occupation of out-of-plane phonon modes, as shown by the larger out-of-plane RMSD than the in-plane RMSD at the ground state (Supplementary Note 4). The excitation was simulated by a sudden electronic temperature jump at time zero from 300 to 3,000 K. The results shows a fast and significant increase of in-plane RMSD within 1 ps but a slow and small rise of RMSD within 10 ps (Supplementary Fig. 2), consistent with the NAQMD simulations. The preferred energy relaxation along the in-plane direction at short times after excitation can be

understood as the reduced density of out-of-plane phonon states in monolayer crystals[35].

Discussion

We now discuss the change of the intralayer spacing between W and Se atomic planes within the monolayer upon optical excitation. We first present the bulk response as a reference. The intralayer dynamics of an exfoliated, 50-nm-thick WSe_2 crystal was measured by monitoring the 004 Bragg peak upon excitation of the same 650 nm light pulses with an incident fluence of 9 mJ cm^{-2}. We found the diffraction peak intensity increases whereas the peak position does not shift (Fig. 3d), indicating a dominant atomic motion in the unit cell within 5 ps, rather than a unit-cell size change that occurs at a later time due to strain wave propagation[24], or the transient tilting of the sample upon optical excitation. By calculating the structure factor as a function of the intralayer spacing, the diffraction intensity change of 8% corresponds to an intralayer contraction of 1.4%, which is a 0.02 Å decrease of lattice spacing of the W–Se layers. The intralayer contraction agrees with the NAQMD simulation shown in Fig. 4c. Assuming a linear dependence of the d-spacing change on the pump fluence, we estimate a symmetric intralayer spacing change of 0.2% in the bulk, with the pump fluence of 1.5 mJ cm^{-2} as used in the monolayer study. This value has been used in the qualitative analysis of differential CTRs.

The model-assisted fitting of the differential CTR of monolayer crystals can yield the intralayer spacings between W–Se layers if they were set as fitting parameters during the fitting procedure. However, the fitting cannot converge for non-zero symmetric intralayer spacing changes that increase or decrease the same amount. We then considered modelling the intralayer spacing independently as d_{bot} and d_{top}, referring to the spacing between the top or bottom of Se layers to the middle W layer (Fig. 3c). Based on the intralayer change in the bulk, we constrained $\Delta d_{bot} = 0.2\%$. The fitting procedure converged and yielded $\Delta d_{top} = -0.25 \pm 0.02\%$. The systematical studies of the influence of structural parameters on differential CTRs showed that the asymmetric d-spacing change is required to fit the data, when considering a non-zero intralayer spacing change (Supplementary Note 2). This indicates that the asymmetric infrared active mode A_2'' is dominantly excited in monolayer crystals in contrast to the excitation of the A_{1g} mode in the bulk[35], which may be attributed to the breaking of the mirror symmetry with respect to W layers due to the influence of substrate. The attempt to take account of the substrate influence in the NAQMD simulation by introducing one unit-cell-thick Al_2O_3 under WSe_2 (Fig. 4a) does not show a significant asymmetric change of intralayer spacing (Fig. 4c), in comparison with the observed opposite sign change of intralayer spacing. This is potentially due to the one-unit-cell-thick substrate in the model. Simulations containing thicker substrates are computationally challenging and beyond the scope of this work.

Conclusions

We demonstrated the femtosecond surface X-ray diffraction to study the nonequilibrium structural dynamics of monolayer crystals on a supporting substrate. Upon optical excitation, we characterized both in-plane and out-of-plane atomic motions in monolayer WSe_2 crystals. We found that energy relaxation in the lattice occurs anisotropically, favouring the in-plane over the out-of-plane direction. The corresponding intralayer spacing changes in monolayer crystals are asymmetric, with Se atoms moving in the same direction with respect to W atoms, potentially due to the influence of the substrate, and is in contrast to the symmetric intralayer lattice contraction in bulk crystals. These measurements enabled the direct comparison to nonadiabatic quantum molecular dynamics simulations which largely reproduce the observations. The general understanding of ultrafast optoelectronic processes under intense optical excitation may need to be reevaluated to take into account the change of the lattice degrees of freedom. The demonstrated femtosecond surface X-ray diffraction opens new opportunities for a direct characterization of nonequilibirum lattice structures at and across the interface of a wide range of low-dimensional material systems. Similar approaches including experimental set-up and data analysis may benefit the design of similar studies using ultrafast electron diffraction as well.

Online content

Any methods, additional references, Nature Research reporting summaries, source data, statements of data availability and associated accession codes are available at https://doi.org/10.1038/s41566-019-0387-5.

Received: 29 August 2018; Accepted: 5 February 2019;
Published online: 11 March 2019

References

1. Novoselov, K. S., Mishchenko, A., Carvalho, A. & Castro Neto, A. H. 2D materials and van der Waals heterostructures. *Science* **353**, aac9439 (2016).
2. Ajayan, P., Kim, P. & Banerjee, K. Two-dimensional van der Waals materials. *Phys. Today* **69**, 38–44 (September, 2016).
3. Chernikov, A., Ruppert, C., Hill, H. M., Rigosi, A. F. & Heinz, T. F. Population inversion and giant bandgap renormalization in atomically thin WS_2 layers. *Nat. Photon.* **9**, 466–470 (2015).
4. Langer, F. et al. Lightwave-driven quasiparticle collisions on a subcycle timescale. *Nature* **533**, 225–229 (2016).
5. Rivera, P. et al. Valley-polarized exciton dynamics in a 2D semiconductor heterostructure. *Science* **351**, 688–691 (2016).
6. Sun, Y., Wang, R. & Liu, K. Substrate induced changes in atomically thin 2-dimensional semiconductors: Fundamentals, engineering, and applications. *Appl. Phys. Rev.* **4**, 011301 (2017).
7. Nika, D. L. & Balandin, A. A. Two-dimensional phonon transport in graphene. *J. Phys. Condens. Matter* **24**, 233203 (2012).
8. Frigge, T. et al. Optically excited structural transition in atomic wires on surfaces at the quantum limit. *Nature* **544**, 207–211 (2017).
9. Balandin, A. A. et al. Superior thermal conductivity of single-layer graphene. *Nano Lett.* **8**, 902–907 (2008).
10. Ghosh, S. et al. Dimensional crossover of thermal transport in few-layer graphene. *Nat. Mater.* **9**, 555–558 (2010).
11. Lee, J. J. et al. Interfacial mode coupling as the origin of the enhancement of T_c in FeSe films on $SrTiO_3$. *Nature* **515**, 245–248 (2014).
12. Chow, C. M. et al. Unusual exciton–phonon Interactions at van der Waals engineered interfaces. *Nano Lett.* **17**, 1194–1199 (2017).
13. Jin, C. et al. Interlayer electron–phonon coupling in WSe_2/hBN heterostructures. *Nat. Phys.* **13**, 127–131 (2017).
14. Gerber, S. et al. Femtosecond electron–phonon lock-in by photoemission and X-ray free-electron laser. *Science* **357**, 71–75 (2017).
15. Raman, R. K. et al. Direct observation of optically induced transient structures in graphite using ultrafast electron crystallography. *Phys. Rev. Lett.* **101**, 077401 (2008).
16. Lin, M.-F. et al. Ultrafast non-radiative dynamics of atomically thin $MoSe_2$. *Nat. Commun.* **8**, 1745 (2017).
17. Waldecker, L. et al. Momentum-resolved view of electron–phonon coupling in multilayer WSe_2. *Phys. Rev. Lett.* **119**, 036803 (2017).
18. Cremons, D. R., Plemmons, D. A. & Flannigan, D. J. Femtosecond electron imaging of defect-modulated phonon dynamics. *Nat. Commun.* **7**, 11230 (2016).
19. Cremons, D. R., Plemmons, D. A. & Flannigan, D. J. Defect-mediated phonon dynamics in TaS_2 and WSe_2. *Struct. Dyn.* **4**, 044019 (2017).
20. Ruan, C.-Y., Vigliotti, F., Lobastov, V. A., Chen, S. & Zewail, A. H. Ultrafast electron crystallography: transient structures of molecules, surfaces, and phase transitions. *Proc. Natl Acad. Sci. USA* **101**, 1123–1128 (2004).
21. Ruan, C.-Y., Lobastov, V. A., Vigliotti, F., Chen, S. & Zewail, A. Ultrafast electron crystallography of interfacial water. *Science* **304**, 80–84 (2004).
22. Mannebach, E. M. et al. Dynamic structural response and deformations of monolayer MoS_2 visualized by femtosecond electron diffraction. *Nano Lett.* **15**, 6889–6895 (2015).
23. Hu, J., Vanacore, G. M., Cepellotti, A., Marzari, N. & Zewail, A. H. Rippling ultrafast dynamics of suspended 2D monolayers, graphene. *Proc. Natl Acad. Sci. USA* **113**, E6555–E6561 (2016).
24. Mannebach, E. M. et al. Dynamic optical tuning of interlayer interactions in the transition metal dichalcogenides. *Nano Lett.* **17**, 7761–7766 (2017).
25. Shen, Y. Phase-sensitive sum-frequency spectroscopy. *Annu. Rev. Phys. Chem.* **64**, 129–150 (2013).

26. Jones, A. M. et al. Excitonic luminescence upconversion in a two-dimensional semiconductor. *Nat. Phys.* **12**, 323–327 (2016).
27. Mishra, H., Bose, A., Dhar, A. & Bhattacharya, S. Exciton–phonon coupling and band-gap renormalization in monolayer WSe_2. *Phys. Rev. B* **98**, 045143 (2018).
28. Poellmann, C. et al. Resonant internal quantum transitions and femtosecond radiative decay of excitons in monolayer WSe_2. *Nat. Mater.* **14**, 889–893 (2015).
29. Zhu, H. et al. Observation of chiral phonons. *Science* **359**, 579–582 (2018).
30. Robinson, I. K. & Tweet, D. J. Surface X-ray diffraction. *Rep. Prog. Phys.* **55**, 599–651 (1992).
31. Brivio, J., Alexander, D. T. L. & Kis, A. Ripples and layers in ultrathin MoS_2 membranes. *Nano Lett.* **11**, 5148–5153 (2011).
32. Meyer, J. C. et al. The structure of suspended graphene sheets. *Nature* **446**, 60–63 (2007).
33. Shimojo, F. et al. Large nonadiabatic quantum molecular dynamics simulations on parallel computers. *Comput. Phys. Commun.* **184**, 1–8 (2013).
34. Sadasivam, S., Chan, M. K. & Darancet, P. Theory of thermal relaxation of electrons in semiconductors. *Phys. Rev. Lett.* **119**, 136602 (2017).
35. Ataca, C., Topsakal, M., Aktürk, E. & Ciraci, S. A comparative study of lattice dynamics of three- and two-dimensional MoS_2. *J. Phys. Chem.* **115**, 16354–16361 (2011).

Acknowledgements

I.-C.T., Q.Z., K.S., G.C., X.X. and H.W. acknowledge support from the Department of Energy, Office of Science, Office of Basic Energy Sciences, Materials Sciences and Engineering Division, under contract no. DE-SC0012509. A.K., H.K., A.N., F.S., R.K.K. and P.V. acknowledge support of the Computational Materials Sciences Program funded by the US Department of Energy, Office of Science, Basic Energy Sciences, under Award Number DE-SC0014607. E.M.M., C.N., A.M.L. and T.F.H. acknowledge support by the Department of Energy, Office of Science, Basic Energy Sciences, Materials Sciences and Engineering Division, under contract DE-AC02-76SF00515. F.E. gratefully acknowledges grant LPDS 2013-13 from the German National Academy of Sciences Leopoldina. NAQMD simulations were performed at the Argonne Leadership Computing Facility under the Department of Energy, the Innovative and Novel Computational Impact on Theory and Experiment Program and at the Center for High Performance Computing of the University of Southern California. Use of the Linac Coherent Light Source, SLAC National Accelerator Laboratory, is supported by the US Department of Energy, Office of Science, Office of Basic Energy Sciences under contract no. DE-AC02-76SF00515. Work at the Advanced Photon Source and the Center for Nanoscale Materials was supported by the US Department of Energy, Office of Science, under contract no. DE-AC02-06CH11357. S.Sa. was supported by Laboratory Directed Research and Development (LDRD) funding from Argonne National Laboratory.

Author contributions

I.C.T., H.Z., Q.Z., K.S., E.M., C.N., F.E., D.Z., J.G., M.K., S.Song, S.N., T.H., X.X., A.L. and H.W. performed the experiments. A.K. H.K., F.S., R.K., R.V., A.N., S. Sadavisam and P.D. performed first-principles calculations. K.S., G.C. and X.X. made samples. I.C.T. and H.W. wrote the manuscript with contributions from all authors. H.W. and X.X. conceived this study.

Competing interests

The authors declare no competing interests.

Additional information

Supplementary information is available for this paper at https://doi.org/10.1038/s41566-019-0387-5.

Correspondence and requests for materials should be addressed to H.W.

Methods

Sample preparation and static surface X-ray diffraction. Monolayer WSe_2 crystals were grown using a physical vapour transport method[36]. They were transferred to the Al_2O_3 substrate with isotropic in-plane crystallite orientations. The regions of the samples with monolayer coverage over 95% (grey colour, Fig. 1a inset) were selected for the study. The small contribution from multilayer crystals <3 nm-thick (white colour, Fig. 1a inset) did not alter the measured CTR profile and thus was not included in the model-assisted data analysis. Preliminary surface X-ray diffraction studies were carried out at the Advanced Photon Source. A typical grazing-incidence diffraction pattern from monolayer WSe_2 on a sapphire substrate is shown on the flat area detector as tilted streaks in Fig. 1a. A data correction procedure[37] is applied to obtain the diffraction intensity distribution in reciprocal space (Fig. 1b). Since the in-plane lattice constant of WSe_2 is different from Al_2O_3 substrate, the monitored off-specular {10l} CTR has no contribution from the Al_2O_3 substrate, which allows independent analysis of the monolayer structural properties without interference with the substrate[38]. The {10l} CTR of the monolayer can then be discretely mapped by integrating the corrected diffraction pattern at different q_z values (Fig. 1b)[39].

Femtosecond surface X-ray diffraction. Femtosecond X-ray scattering measurement were performed in grazing incident geometry at the X-ray Pump-Probe (XPP) instrument at the Linac Coherent Light Source (LCLS). The samples were kept under helium atmosphere during the measurements. The monochromatic X-ray beam with a photon energy of 9.55 keV and 50 fs pulse duration stroke the sample surface at a grazing angle, $\alpha = 1°$ shown in Fig. 1a. The large X-ray beam footprint resulting from grazing incidence geometry also serves to spread the X-ray beam with the cross-section full-width at half-maximum of $50 \times 50\,\mu m$ to minimize the sample degradation. The diffracted intensity was then detected by an area detector: Cornell-SLAC Pixel Array Detector (CSPAD). The distance between sample and detector was 431 mm, calibrated by a LaB_6 diffraction pattern. The linearly polarized pump light pulses were derived from an optical parametric amplifier with a wavelength of 650 nm and 200 μm in diameter, close to the absorption peak of the B-exciton of monolayer WSe_2[40]. Although the incident fluence of 1.5 mJ cm^{-2} was relatively strong, the absorption of optical energy in monolayer WSe_2 corresponds only to an absorbed fluence of 6.2 μJ cm^{-2} (that is, electron density of 1.3×10^{13} cm^{-1}), calculated based on the monolayer optical reflectivity and complex dielectric constant[40]. The crossing angle between the laser and X-ray pulses was 5° in the horizontal plane and the X-ray scattering was in the vertical plane. The temporal resolution was limited by the pump–probe timing jitter on the order of 100 fs. The X-ray diffraction pattern were collected as a function of the pump–probe delay in a mode with laser-on and laser-off alternating at a 60 Hz repetition rate. The time-dependent reciprocal space maps were analysed to measure the structural dynamics of the monolayer crystals. The sensitivity of the measurement depends on sample quality, experimental geometry and signal-to-noise ratio. Compared to the static measurements, the use of lock-in detection in this pump–probe measurement offers enhanced sensitivity for measuring the relative change of the CTRs. In this study, the changes of RMSD upon excitation were measured with an uncertainty of 0.002 Å.

Nonadiabatic quantum molecular dynamics simulations. Nonadiabatic quantum molecular dynamics (NAQMD) simulations were performed on a simulation cell containing 3×3 unit cells of WSe_2 monolayer in the 2H crystal structure (9 formula units = 27 atoms) supported on a sapphire (0001) surface. Simulations of free WSe_2 monolayers were performed in simulation cells containing 3×3 unit cells of WSe_2 suspended in vacuum. All simulations were performed using a highly parallelized plane-wave density functional theory (DFT) program developed in-house, which can efficiently calculate long-range exact exchange corrections and excited-state forces[41].

Electronic structures were described in the framework of DFT[42,43], and the generalized gradient approximation was used for the exchange-correlation term[44]. Valence wavefunctions were calculated by projector augmented-wave method[45], and projector functions were generated for the 4*s*, 4*p* and 4*d* states of selenium, 5*d*, 6*s* and 6*p* states of tungsten, 3*s*, 3*p* and 3*d* states of aluminium, and 2*s* and 2*p* states of oxygen, respectively. The DFT-D method was used to approximate van der Waals interactions in the system[46]. The electronic pseudo-wave functions and pseudo-charge density were expanded by plane waves with cut-off energies of 30 Ry and 250 Ry, respectively. All NAQMD simulations were performed in the NVT ensemble with an external Nose–Hoover thermostat at 300 K and equations of motion are integrated with a time step of 0.97 fs.

Data availability

The data that support the plots within this paper and other findings of this study are available from the corresponding author upon reasonable request.

References

36. Clark, G. et al. Vapor-transport growth of high optical quality WSe_2 monolayers. *APL Mater.* **2**, 101101 (2014).
37. Jiang, Z. Gixsgui: a matlab toolbox for grazing-incidence X-ray scattering data visualization and reduction, and indexing of buried three-dimensional periodic nanostructured films. *J. Appl. Cryst.* **48**, 917–926 (2015).
38. Renaud, G. Oxide surfaces and metal/oxide interfaces studied by grazing incidence X-ray scattering. *Surf. Sci. Rep.* **32**, 5–90 (1998).
39. Mannsfeld, S. C. B., Virkar, A., Reese, C., Toney, M. F. & Bao, Z. Precise structure of pentacene monolayers on amorphous silicon oxide and relation to charge transport. *Adv. Mater.* **21**, 2294–2298 (2009).
40. Li, Y. et al. Measurement of the optical dielectric function of monolayer transition-metal dichalcogenides: MoS_2, $MoSe_2$, WS_2, and WSe_2. *Phys. Rev. B* **90**, 205422 (2014).
41. Shimojo, F. et al. A divide-conquer-recombine algorithmic paradigm for large spatiotemporal quantum molecular dynamics simulations. *J. Chem. Phys.* **140**, 18A529 (2014).
42. Hohenberg, P. & Kohn, W. Inhomogeneous electron gas. *Phys. Rev.* **136**, B864–B871 (1964).
43. Kohn, W. & Sham, L. Self-consistent equations including exchange and correlation effects. *Phys. Rev.* **140**, A1133–A1138 (1965).
44. Perdew, J. P., Burke, K. & Ernzerhof, M. Generalized gradient approximation made simple. *Phys. Rev. Lett.* **77**, 3865–3868 (1996).
45. Blöchl, P. E. Projector augmented-wave method. *Phys. Rev. B* **50**, 17953–17979 (1994).
46. Grimme, S. Semiempirical GGA-type density functional constructed with a long-range dispersion correction. *J. Comput. Chem.* **27**, 1787–1799 (2006).